RESEARCH ARTICLE

Efficient Bidirectional Wireless Power Transfer System Control Using Dual Phase Shift PWM Technique for Electric Vehicle Applications

MURUGAN VENKATESAN[1], R. NARAYANAMOORTHI[1], (Member, IEEE), KAREEM M. ABORAS[2], AND AHMED EMARA[3,4]

[1]Wireless Charging Research Centre, Department of Electrical and Electronics Engineering, SRM Institute of Science and Technology, Kattankulathur 603 203, India
[2]Department of Electrical Power and Machines, Faculty of Engineering, Alexandria University, Alexandria 21544, Egypt
[3]Electrical Engineering Department, University of Business and Technology, Ar Rawdah, Jeddah 23435, Saudi Arabia
[4]Engineering Mathematics and Physics Department, Faculty of Engineering, Alexandria University, Alexandria 21544, Egypt

Corresponding authors: R. Narayanamoorthi (narayanamoorthi.r@gmail.com) and Ahmed Emara (a.emara@ubt.edu.sa)

ABSTRACT The emerging bidirectional wireless power transfer (BWPT) technology provides improved flexibility without requiring human intervention by facilitating smooth Grid to Vehicle (G2V) and Vehicle to Grid (V2G) operations. Nevertheless, BWPT systems have issues with power factor management, efficiency, and power transfer rate. In order to address these issues, sophisticated control systems are essential. While unidirectional Wireless Power Transfer (WPT) are adequately managed by conventional control techniques and power factor corrector (PFC) approaches, whereas bidirectional systems require dual-side control of power converters in order to efficiently handle G2V and V2G operations. Furthermore, the existing literature predominantly focuses on power factor improvement for unidirectional WPT systems. This paper presents a dual-phase shift Pulse Width Modulation (PWM) technique for an improved PFC control for BWPT. A thorough analysis of the suggested approach is conducted, looking into power factor, bifurcation, total harmonic distortion (THD), and power losses. Experimentation and verification together with simulation studies at an operating frequency of 85 kHz and a power rating of 3.7 kW demonstrate the effectiveness of the system. Dual-phase shift control yields 94.4% power transfer efficiencies in simulations and 90.1% in experimental results in both power transfer directions.

INDEX TERMS Bidirectional charging, electric vehicle, wireless power transfer, vehicle to grid, coil structure, bidirectional DC/DC converters, smart charging.

I. INTRODUCTION

The automotive industry is significantly impacted by the advent of new energy challenges that are fueled by environmental concerns and the depletion of fossil fuels. This effect has prompted more study and advancement in the field of EVs [1]. One of the most important issues that needs to be resolved to enhance industry growth is EV recharging. The main difficulties with EV charging are recharge time, safety, and human interaction. To overcome these issues, the newly developed

The associate editor coordinating the review of this manuscript and approving it for publication was Diego Masotti.

WPT technology is essential since it transfers power from a source to a load without physical contact [2]. In contrast to conventional cable charging, WPT offers the customer far greater comfort and security. With the use of this technology, charging is now safer and more convenient as there is no need for charging wires. Users may charge their devices anywhere there is a charging outlet thanks to human intervention-free charging features, which also minimize the size and weight of batteries and charging intervals [3]. Furthermore, WPT technology finds uses in high-power applications like as underwater vehicles, railway traction, and wireless energizing of implanted devices in the medical field [4], [5]. It is not

limited to EV charging. WPT is significant because it can get beyond the limitations of battery-powered devices, such as short battery life and expensive starting expenditures. The characteristics of WPT, including its dependability, convenience, safety, and resilience to weather, have increased its appeal [6]. Specifically, it is expected that the use of BWPT will accelerate advancements in V2H, V2V, and V2G technologies, allowing electricity to flow both ways. For high-frequency operation, fully controlled switching components, such as SIC MOSFETs and IGBTs, are incorporated into the design of the WPT/BWPT systems for both the primary and secondary bridges. The usual block diagram showing how photovoltaic (PV) systems, wirelessly connected EVs, a DC bus, and the power grid interact in V2G and G2V operations is shown in Figure 1. EVs contribute to the power grid by providing active or reactive power compensation capabilities, enhancing power quality and grid stability [7]. The integration of Renewable Energy Systems (RES), EVs, and the power grid can effectively increase RES penetration [8]. However, this integration requires constant bidirectional communication during charging and discharging condition.
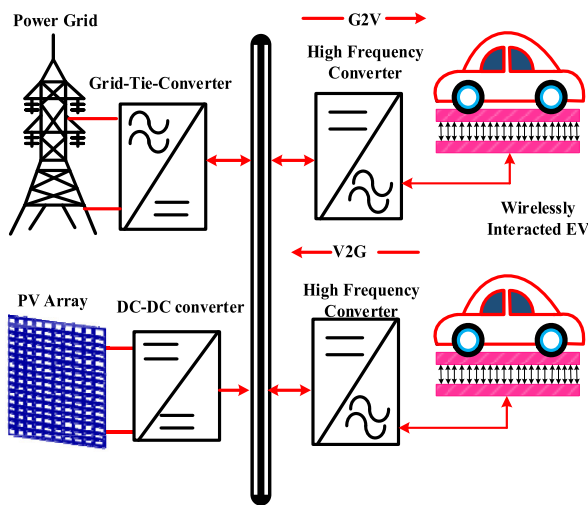

FIGURE 1. Illustration of wirelessly interconnected EVs in the V2G and G2V service.

The grid-connected system also needs to maintain the THD and the power factor within the allowable range. Also, the power electronic converters used in the wireless charging system play a crucial role in maintaining the power quality. In the WPT system, different uncertain scenarios such as misalignment, parameter detuning, coil distance variation, and load variation introduce deviation from the normal operation of the system [9]. It also brings soft switching loss, power factor reduction, component stress, and power transfer efficiency reduction. Nevertheless, the power factor is more important for the BWPT system to maintain the grid integration. Hence, maintaining a higher power factor is very important for the wireless charger design. On the other hand, the power transfer efficiency can be improved by using suitable resonant compensation networks at the primary

and secondary [10]. Various compensation topologies are proposed for the unidirectional system to maintain the voltage and current variation. The two bridges' AC links usually have compensating tanks added to them to increase system transmission capacity and efficiency. Attention has been drawn to the LCC-BWPT system because of its symmetrical structure and less sensitivity to load change and coupling coefficient [11]. The LCC compensation architecture is used to alleviate problems resulting from S compensation on the primary side [12]. Through the utilization of an inverter to transform a voltage source into a current source, the LCC resonance compensation circuit on the primary side ensures a consistent current in the primary coil, preventing overcurrent concerns associated with S compensation. Additionally, even under light loads, the LCC resonance correction circuits contribute to the elevation of the output voltage. The relative phase angle and amplitude of the voltages produced by full-bridge inverters on the main and secondary sides control the power flow direction as well as the magnitude of both real and reactive power flows in classic BWPT [13]. Wireless communication interfaces can be used to synchronize the switching signals of these inverters, however doing so lowers system robustness and raises system expenses. An alternate control technique described obviates the necessity for wireless communication by synchronizing using the active and reactive power of the secondary side's full-bridge inverter [14], [15]. The Real and reactive power flows are still determined by the passive elements' characteristics as well as the relative phase angle and voltage magnitude from the full-bridge inverters on both sides. Recent advancements have shifted from single-sided to double-sided compensation in wireless circuit designs, providing greater flexibility and meeting WPT system design criteria [15]

For WPT systems operating at higher frequencies, especially in charging EV batteries, power regulation from unregulated AC output to regulated DC output is crucial. In this context, Integrated Power Factor Correction (PFC) circuits have been proposed to enhance system power density, replacing traditional front-end PFC circuits that often require cumbersome passive components [16]. Despite the potential impact on battery life, the integration of EVs with other resources is anticipated to be financially advantageous for both grid operators and EV owners. To enhance overall system cost-effectiveness, Power Factor Correction (PFC) has been implemented on the secondary side of a WPT system [17]. However, it's crucial to acknowledge that this approach introduces increased circuit complexity [2]. The control strategy introduced for the secondary side of a WPT system employing an LCCL network underscores the significance of the LCCL compensation topology in maintaining a stable output voltage on the secondary side. Similarly, the stability is crucial for efficiently governing the connected DC–DC converter responsible for battery charging [3]. To manage the output voltage in a WPT system, a hybrid Inductor-Capacitor-Capacitor-Series (LCC-S) compensated approach is employed [18]. By combining phase shift modulation

and switch-controlled capacitor, this technique known as the LCC-S compensated WPT allows for wide-range output voltage regulation across the complete voltage range [4], [18], and [19]. For validation purposes, a 500-W prototype with a 400-V input voltage and a 100-250-V output voltage was assembled. Experimental data show that the converter maintains Zero Voltage Switching (ZVS) over the voltage range and reaches a maximum efficiency of 94.1% [19]. A detailed analysis of a dual-side LCC-LCC compensated WPT converter was done to obtain load-independent Constant Voltage (CV) and Constant Current (CC) outputs at two distinct sites of zero-phase angular frequencies [5]. This analysis offered a methodical approach to design. Weight and volume are reduced with this technology in comparison to typical WPT topologies. The method streamlines its control system by enabling CC and CV power transfer modes through the use of contemporary Analog Phase Control (APC) and Digital Phase Control (DPC) techniques [6], [7]. A combination of simulation analysis and experimental data has been used to verify the accuracy of this novel approach. Examining secondary active converters as a means of controlling power transfer in WPT systems demonstrates that traditional WPT circuits frequently employ a front-end PFC interface, resulting in sizable passive components that have a substantial effect on system dependability, losses, and volume. Because there are no intermediary storage elements on the primary side, phase shifts between the primary and secondary bridges are usually calculated using sophisticated synchronization techniques [7]. A new phase-shift control system was devised for a Full-Bridge Active Rectifier (F-BAR) functioning in Bidirectional Wireless Power Transfer (BWPT). This required modifications to the conventional receiver-side rectifier design. Theoretical and simulation findings show how this innovative control technique permits output value control without requiring a connection between the transmitter and receiver. Supplying the input voltage of 325V DC, an output power range of 0 to 3.7 kW, and a maximum efficiency of 94.4% is achieved. The experimental validation verifies the effectiveness of the converter and proposed control technique. The major contributions of the paper are

- The dual-side phase shift-controlled techniques control the power flow as well as improve the power factor.
- The performance analysis such as frequency bifurcation, power loss, and THD of proposed techniques for the BWPT system.
- The simulation and experimental validation of the dual side phase shift control technique for the BWPT system.

Section II outlines different modes of operation in BWPT, while Section III delves into various control techniques for BWPT, emphasizing phase shift control. Section IV delineates the modes of bidirectional power flow control between V2G and G2V. Section V provides detailed information on the design parameters and components of a 3.7 kW system, and Section VI offers an illustration for evaluating the performance of the BWPT system under both scenarios. PFC is integrated within the resonant converter, with one

strategy implemented on the primary side and the other on the secondary side. The evaluation primarily focuses on key parameters such as power losses, THD, and efficiency.

II. BIDIRECTIONAL WPT SYSTEM

In the BWPT system, EVs are connected to the DC bus via the WPT charging system. Each side of the system consists of coupling coils, high-frequency converters, a compensation circuit, and controllers with specialized designs. Figures 2 and 3 illustrate the circuit diagram of the proposed topology during both charging and discharging conditions. During the transfer of energy from the grid to the EV in G2V Mode, the primary converter operates as a DC/AC inverter, while the secondary converter serves as a controlled rectifier for AC/DC conversion. Conversely, in V2G mode, when the EV battery transfers power to the grid, the roles of the converters are reversed [11]. The circuit comprises a primary side inverter with an LCC-based resonant converter and a secondary side converter. By adjusting the primary side voltage (V_P) or secondary end voltage (V_S) in this bidirectional control architecture by matching the duty cycles of the inverters the regulation is accomplished. Modulating the low-frequency signal average value of the primary side as well as secondary end voltages allows for power regulation. The system includes both primary and secondary compensation networks, as was previously described.
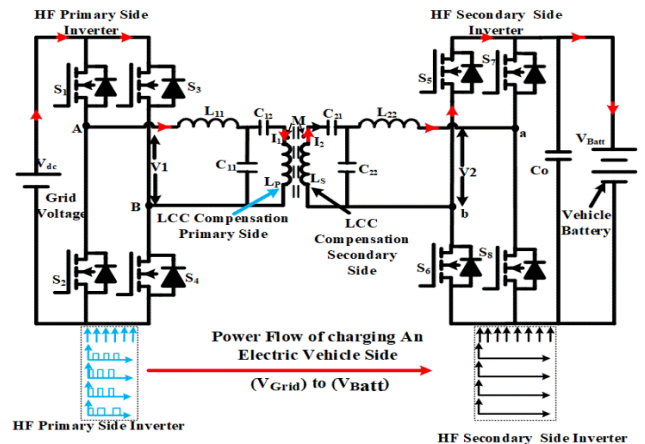

FIGURE 2. BWPT system for the Operation of (V_{Grid}) Side to (V_{Batt}) Side.

The exchange of energy from the primary coil to the secondary coil is made possible through the application of mutual induction principles, which take place during the resonance condition. The controllers play a crucial role in overseeing the power transfer between the two coils throughout each operational phase. Phase shift control is commonly employed through an improved Pulse Width Modulation (PWM) technique, where control signals are directed to both sides of the converter switches. To implement bidirectional converters, fundamental approaches consider the dual functionality of both converters at primary and secondary parts. When transferring power from the grid to the battery,
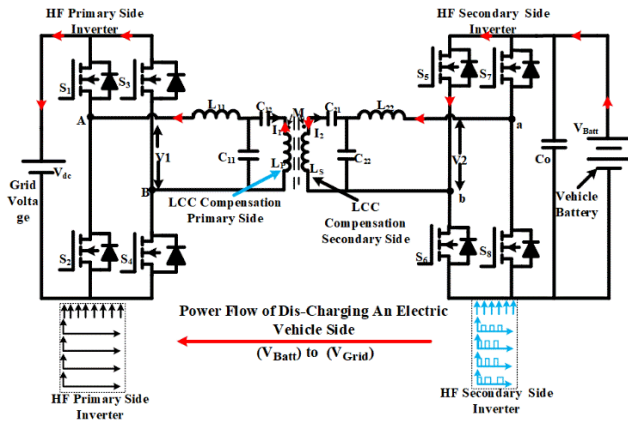
FIGURE 3. BWPT system for the Operation of (V_{Batt}) Side to (V_{Grid}) Side.

FIGURE 4. Equivalent circuit of presented BWPT operation in Mode I.

FIGURE 5. Equivalent circuit of presented BWPT operation in Mode II.

Phase Shifting Modulation (PSM) techniques are employed to regulate the primary converter, while the secondary side converter functions as a rectifier simultaneously. Figure 2 illustrates this methodology. Likewise, during the transfer of power from the battery to the grid, the DC/AC converter on the secondary side operates as an inverter, while the AC/DC converter on the primary side functions as a rectifier. This is illustrated in Figure 3, depicting the discharge process. In this method, the active power flow is easily modifiable, and the anticipated efficiency is determined. To establish the configuration in both controllers, the power converters must work in conjunction. This is achieved by establishing a wireless communication channel, with signal processing delay not being a limiting factor. Thus, both controllers are readily configurable and synchronized.

A. MODES OF OPERATION OF BWPT

Mode I: (α to π)

During the time interval (αt to π), switches (S_1) and (S_4) are conducting on the primary side, allowing current to flow through (S_1), compensating inductance (L_{f1}), series and parallel capacitances (C_1, C_{f1}), and the primary coil (L_1). Simultaneously, switches (S_4) are also part of this circuit. On the secondary side, switches (S_7) and (S_6) are active during the same period. The induced current flows through the secondary coil (L_2), series and parallel capacitances (C_2, C_{f2}), compensating inductance (L_{f2}), and the switches (S_7) and (S_6), eventually reaching the load.

The current flows in the forward direction across the load on the vehicle battery side. Figure 4 depicts the equivalent circuit of the described bidirectional power transfer system functioning in Mode I.

Mode II: ($0 \leq t \leq \alpha$)

During the time interval (0 to α), the upper switches on the primary side, namely (S_1) and (S_3), are conducting. However, some dead time occurs due to the release of stored energy in the inductance, causing the current to circulate between these two switches, resulting in a zero-current state. Simultaneously, on the secondary side during the same period,
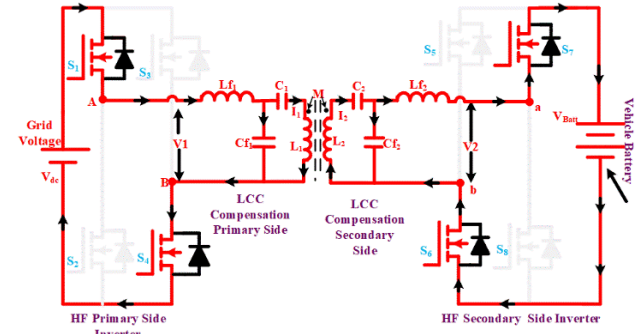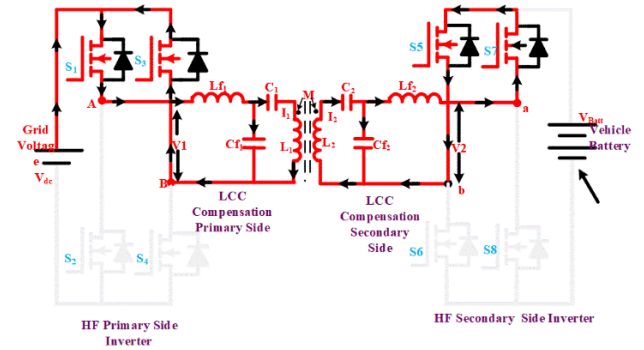
the upper switches (S_5) and (S_7) are conducting. Similar to the primary side, there exists a dead time when the stored energy in the inductance releases current, circulating between switches (S_5) and (S_7). As a result, the current through the load becomes zero [14]. Figure 5 provides a visual representation of the equivalent circuit of the presented bidirectional power transfer system in operation during Mode II.

Mode III: ($\pi + \alpha \leq t \leq 2\pi$):

During the time interval ($\pi + \alpha t$ to 2π), switches (S_2) and (S_3) are conducted on the primary side. The current (I) flows through switches (S_2), compensating inductance (L_{f1}), series and parallel capacitance (C_1, C_{f1}), the primary coil (L_1), and the switches(S_3). Simultaneously, on the secondary side during the same period, switches(S_8) and (S_5) are conducting. The induced current flows through the secondary coil (L_2), series and parallel capacitance's (C_2, C_{f2}), compensating inductance (L_{f2}), and the switches (S_8), the load, and the switches (S_5), respectively.

The current flows through the load on the vehicle battery side in a reversed direction. Figure 6 illustrates the Mode III equivalent circuit operation.

Mode IV:($\pi \leq t \leq \pi + \alpha$)

During the time interval (π to $\pi + \alpha$), the lower switches on the primary side, namely (S_2) and (S_4), are conducting. However, some dead time occurs due to the release of stored energy in the inductance, leading to the circulation of current
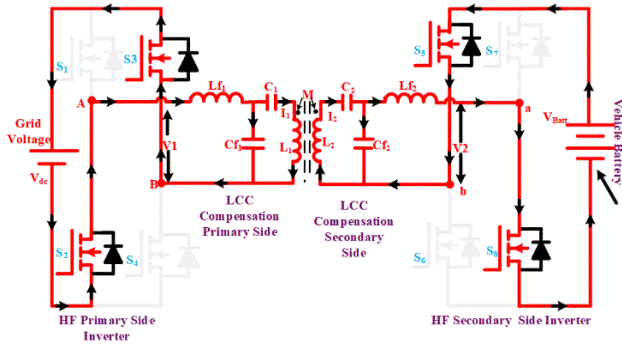
FIGURE 6. Equivalent circuit of presented BWPT operation in Mode III.
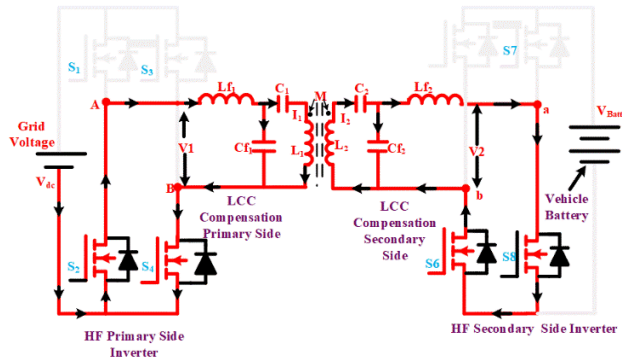

FIGURE 7. Equivalent circuit of presented BWPT operation in Mode IV.

between these two lower switches as a result, the current becomes zero.

Simultaneously, during the same period on the secondary side, the two lower switches, (S₆) and (S₈), are conducting. Similar to the primary side, there is a dead time as the stored energy in the inductance releases current, circulating between switches (S₅) and (S₇), respectively. As a result, the current across the load becomes zero. Figure 7 illustrates the equivalent circuit of the presented bidirectional power transfer system operating in Mode IV. Consequently, the switching waveforms for different modes of bidirectional wireless power transfer for V2G and G2V operations are illustrated in Figure 8.

III. PHASE SHIFT CONTROL

The parameter α, reliant on the reference signal, is crucial for enabling the primary side circuit to operate at the rated current of the secondary controller. It is employed to finely adjust the output voltage of the primary side inverter. Simultaneously, the secondary controller generates the phase shift (β) between the legs of the secondary inverter, influencing the relationship between both primary and secondary output voltages. Implementing the PWM technique involves utilizing low-level switching signals, which are subsequently interpreted for the left- and right-side by fine-tuning of phase shift parameters (α, β, and δ) [16]. To achieve the
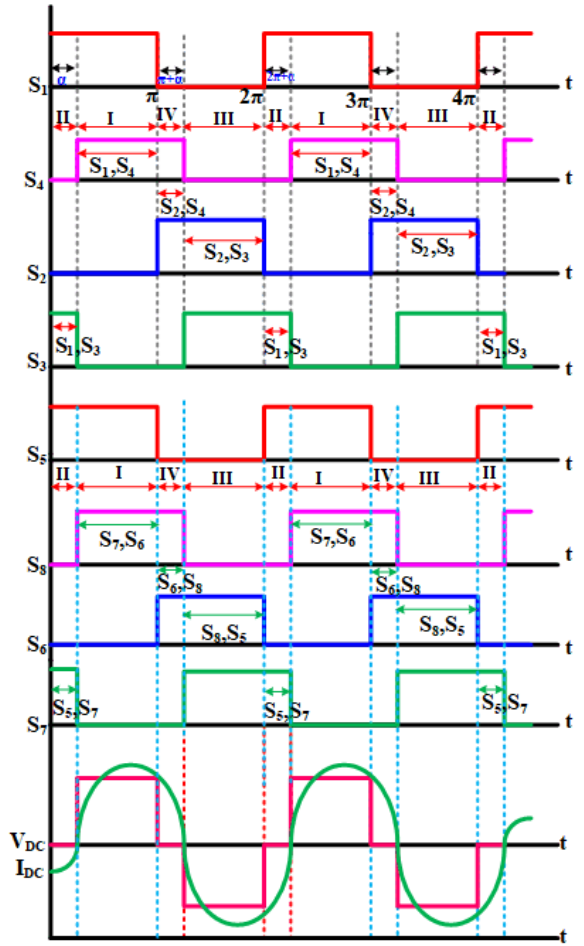

FIGURE 8. Switching waveforms of BWPT for V2G and G2V Operation.

desired magnitude and direction of power flow, it becomes necessary to modify the secondary side control parameters (β and δ). The configuration of the four switches on both sides of the high-frequency converters is defined by signals enhanced by the driver circuits. These control parameters are crucial for attaining the desired power flow within the system, and adjusting the amplitude and phase of the inverter voltages [17].

In BWPT, each side can simultaneously function as both a supply and a load. Consequently, both sides must be treated similarly. Simultaneously engaging the full-bridge converters on both the primary and secondary sides involves a purposeful delay in activating semiconductor switches on both ends. The regulation of power flow between the primary and secondary converters (AC/DC and DC/AC) utilizes phase angles (α, β) and the delay angle (δ). Figure 9 visually represents the switching waveforms, illustrating the phase angle delay between the two converters. Typically, the phase shift angle modulates the power level on both sides. The delay angle (δ) indicates the phase displacement between the peak voltages of the primary and secondary inverters [18]. Both converters
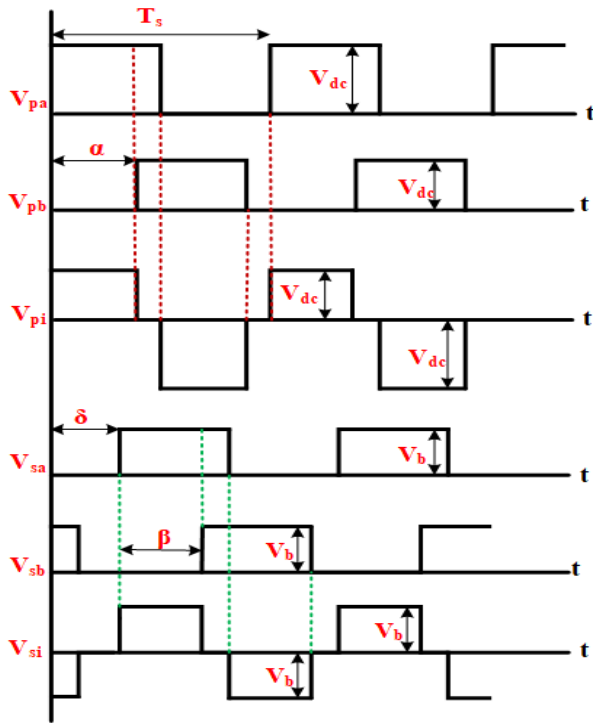
FIGURE 9. Switching waveforms of phase angle delay between the two converters.

output voltage $V_P(t)$ and $V_S(t)$ for the first harmonics are expressed as

$$V_p(t) = \left(\frac{4}{\pi}\right) V_p \sum_{n=1,3}^{\infty} \frac{1}{n} \cos\left(n\omega_r t - \frac{n\alpha}{2}\right) \sin\left(\frac{n\alpha}{2}\right) \quad (1)$$

$$V_s(t) = \frac{4}{\pi} V_s - \sum_{n=1,3}^{\infty} \frac{1}{n} \cos\left(n\omega_r t - \frac{n\alpha}{2} + n\delta\right) \sin\left(\frac{n\beta}{2}\right) \quad (2)$$

where n represents the order of harmonics. In the above equation, α & β represent the phase shift between switches of an inverter pair, and similarly, V_P and V_S represent the primary and secondary side inverter peak voltages, and 'n' represents the harmonics orders.

IV. DESIGN PARAMETERS FOR THE BWPT SYSTEM

Developing the phase shift controller with improved PFC control is essential for the design of BWPT systems. The power transfer between the primary and secondary coils can be expressed at the resonance frequency.

$$P = \omega_0 M I_p I_s \quad (3)$$

The mutual inductance between the primary and secondary coils is denoted by M in this instance. The Root-Mean-Square (RMS) current passing through the primary and secondary coils is indicated by the letters I_P and I_S, respectively. In wireless charging systems, the mutual inductance between these coils is crucial since it directly affects the efficacy and

efficiency of power transfer. In this particular scenario, the operating frequency of 85 kHz aligns with the SAE J2954 standard. Subsequently, the expression for the output power is as follows,

$$P = 2\pi f_0 \left(N_p I_p\right) \left(N_s I_s\right) K \sqrt{\hat{L}_p \hat{L}_s} \quad (4)$$

where f_0 represents the operating frequency. Both the primary and secondary coil turns are indicated by the letters NP and NS, respectively. For both the primary and secondary coils, the inductance per turn is denoted as $\hat{L}_P$ and $\hat{L}_S$, respectively. The coupling coefficient between the coils is represented by K. If K is high, there will be a lower air gap, and vice versa when K is low. The air gap between the charging pads and their size determines the mutual inductance per turn given by the expressions

$$M = K\sqrt{L_p * L_s} \quad (5)$$

The increased mutual inductance (M) results from larger pad diameters and reduced air gap [20]. The self-inductance of the ferrite core is nearly two times as compared to the air core, which increases the coupling coefficient (K) by 30%–50% [21]. Controlling the output power and ampere-turn ratio is essential to ensure that the receiver and transmitter pads are the same size. A 3D finite-element analysis (FEA) model with a lumped coil was created using the charging coil dimensions and air gap to calculate the coupling coefficient and inductance per turn. The ampere-turn design of the primary side and secondary side coils is still an important design element for the specified power rating, air gap, and size [22]. Compared to traditional series compensation, the LCC compensation offers additional design options for current and turn configurations. The LCC-LCC compensating circuit configuration of a connected coil is shown in Figure 2. The current I_P and I_S can be obtained using the following equation

$$I_P = \frac{V_{AB}}{\omega_0 L_{11}}, I_S = \frac{V_{ab}}{\omega_0 L_{22}} \quad (6)$$

Referring to equation (6), for the voltage at input-output, the compensating inductances L_{11} and L_{22} play a role in influencing the currents I_P and I_S. A modification in the value of compensating inductance L_{11} enables a reduction in the coil current I_P. It is possible to determine various coil current ranges (I_P) for a given voltage and to define the number of turns (N_P) with LCC-LCC compensation [23]. When a coil's current is reduced by selecting an excessive number of turns, the coil's inductance and the voltage across it both see a notable increase. Given the insulating layer and turn-to-turn distance of the Litz wire, an exceptionally high voltage may give rise to security and reliability concerns. Furthermore, certain applications may impose restrictions on the system's maximum voltage. As a result, the voltage across the coils and capacitor constrains the number of turns, and this relationship can be mathematically represented by equations (7) and (8).

$$V_{LP} = I_P X_{LP} = j\omega L_p I_p = I_p \left(2\pi N_P^2 \hat{L}_P\right) \quad (7)$$

$$V_{Ls} = I_s X_{Ls} = j\omega L_s I_s = I_s \left(2\pi N_s{}^2 \hat{L}_s\right) \qquad (8)$$

According to the equation above, across the coils the voltage increases by $[2\pi I_p N_p \hat{L}_P]$ for each consecutive turn. The formula for calculating the ratio of input voltage to coil voltage is:

$$G_{vp} = \frac{V_{LP}}{V_{AB}} = \frac{X_{LP}}{XL_{11}} = \frac{L_P}{L_{11}} \qquad (9)$$

After designing the coil and calibrating inductors, the capacitor value can be determined for LCC-LCC compensation by calculating the resonance frequency.

$$\omega_0 = \frac{1}{\sqrt{L_{11}C_{11}}} = \frac{1}{\sqrt{(L_p - L_{11})C_{12}}} \qquad (10)$$

$$\omega_0 = \frac{1}{\sqrt{L_{22}C_{22}}} = \frac{1}{\sqrt{(L_s - L_{22})C_{21}}} \qquad (11)$$

Similarly, the design of the pad is based on three important factors: The current rating of each coil, the number of turns per coil to achieve the necessary self-inductance, and the width of the ferrite core to avoid excessive core loss all contributing to the Litz wire gauge. A comprehensive examination of electrical, magnetic, and thermal characteristics is required to meet the capacitor voltage specifications and inductor current values [24]. To represent the currents passing through an LCC-LCC resonant tank's tuning inductors and primary and secondary coils, use equations (12,13).

$$IL_{11} = \frac{MV_{AB}}{\omega_0 L_{11} L_{22}}, I_{L22} = \frac{MV_{ab}}{\omega_o L_{11} L_{22}} \qquad (12)$$

$$I_{LP} = \frac{V_{AB}}{\omega_o L_{11}}, I_{LS} = \frac{V_{ab}}{\omega_o L_{22}} \qquad (13)$$

In the LCC-LCC resonance compensated systems, the voltages between the tuning capacitors can be calculated as follows by the equation (14) − (15)

$$V_{C12} = \frac{V_{AB}(L_P - L_{11})}{L_{11}} \qquad (14)$$

$$V_{C21} = \frac{V_{ab}(L_s - L_{22})}{L_{22}} \qquad (15)$$

In addition, when considering the heating limitations of the high frequency high-power capacitor must satisfy both the voltage and current requirements. Table 1 displays the actual rating voltages and currents for the proposed design's resonant tank components.

V. POWER FACTOR CORRECTION IN THE BWPT SYSTEM
In an ideal WPT system, Power Factor Correction (PFC) can be implemented either at the front-end or back-end. However, it's crucial to consider that the decision between front-end and back-end PFC depends on various factors, including system requirements, efficiency considerations, and design constraints [25]. Each approach comes with its own set of advantages and disadvantages, and the selection should be made based on specific system needs. In an ideal WPT

TABLE 1. Electrical circuit parameters of 3.7 KW BWPT system.

S: No	Parameters	Symbols	Values
1	Output Power	P_{out}	3.7 kW
2	Input AC voltage	V_{Grid}	325 V
3	Output Converter Voltage	V_{out}	420 V
4	Coupling Co-efficient	K	0.4
5	Switching Frequency	f_s	85 kHz
6	Mutual Inductance	M	46.5μH
7	Capacitor for Primary Side Series Compensation	C_p	31nF
8	Self-Inductance of the Primary Coil	L_P	120 μH
9	Secondary Coil Self Inductance	L_S	120 μH
10	Secondary Side Series Compensation Capacitor	C_S	31nF
11	Capacitance Filter	C_0	30 μF

system, power transfer at the resonant frequency can be expressed as:

$$P_o = \frac{8}{\pi^2} * \frac{V_P * V_S}{\omega * L_M} \qquad (16)$$

The L_M, which is computed using the coupling factor value, the separation between the primary and secondary coils, and the coil misalignment, can be used to calculate the interaction between self and mutual inductance. The letters LP and LS stand for the primary and secondary coils' respective self-inductance. The region of 0.2 to 0.5 is where the K value varies the most. The resonance frequency remains unaffected by the load, and either V_P or V_S can be utilized to adjust the output power. The frequency spectrum outlined by the automotive SAE standard J2954 spans from 81.39 kHz to 90 kHz. The PFC model comprises active rectification, and LCC compensation coupled to an H-bridge converter on both the primary and secondary sides. Additionally, there is passive DC-DC control of the output interfaces for battery charge control. Assuming a correction of the unity power factor, it is considered that power in single-phase alternating current (AC) systems is proportional to the quadratic sine function.

$$p_g(t) = 2V_g I_g \sin(\omega_g t)^2 \qquad (17)$$

where V_g and I_g correspond to the input voltage and RMS current of the grid respectively. Under this condition, the switching frequency is not a control variable. As a result, power control is accomplished by regulating the average low-frequency primary voltage (V_{pf}) or secondary voltage (V_{sf}). This ensures PFC while accommodating a 100 Hz fluctuating power source. Hence, the transferred power can be calculated as follows

$$p_g(t) = V_g I_g = P_{mean}(1 + \cos(2\omega_g t) \qquad (18)$$

It is assumed in this study that continuous voltage (CV) and continuous current (CC) control work together to regulate batteries. We'll use this control mechanism by battery current and voltage measurements. To help with CC management,

a current saturation mechanism has also been included. Accurate current regulation becomes dependent on the internal current control loop, which efficiently offsets internal and external disturbances. Since the resonant current and the secondary-side voltage are always in line, the transmitted power can be computed as follows

$$P = \frac{v_{pf}^{\wedge} * v_{sf}^{\wedge}}{2\omega_0 M} \tag{19}$$

where the fundamental voltage amplitudes on the main and secondary sides at the switching frequency are denoted by $\hat{V}_{pf}$ and $\hat{V}_{sf}$, respectively

$$v_{pf}^{\wedge} = \frac{4}{\pi} V_r \sin(\delta_p \pi/2) \tag{20}$$

$$v_{sf}^{\wedge} = \frac{4}{\pi} V_{BAT} \sin(\delta_s \pi/2) \tag{21}$$

where, δ_p and δ_s represent the primary and secondary duty cycles, respectively. V_r is the rectified grid voltage and V_{BAT} is the battery voltage. Regardless of which converter performs PFC and current shaping, both PFC control strategies necessitate a grid-connected unfolding 50 Hz active rectifier. The resonant inverters control the primary resonant tank (V_P) as well as transfer current between both the primary and secondary coils by manipulating unregulated (AC) voltage. Moreover, communication systems or estimation methods are necessary when the power control is managed by an off-board primary-side resonant inverter.

A. PRIMARY SIDE PSM CONTROL

Primary-side control (PSC) modifies the primary voltage (V_P) to provide control over the battery charging process; the secondary voltage (V_S) is left uncontrolled. To achieve this, a duty-cycle control approach utilizing Phase-Shift Modulation (PSM) is employed within the primary-side resonant inverter. In this setup, all switches are controlled by square modulation, and the phase difference between the two inverter branches regulates the duty cycle (δ_p). To reduce conduction losses on the secondary side, two operational modes are accessible: a passive converter or synchronization with the resonance current. In both cases, it is possible to generate a primary current with a constant magnitude. Both operation modes share a similar duty-cycle calculation approach, with the primary distinction lying in the pulse generation strategy. Furthermore, the pulse patterns for each switching device may vary according to their operational frequency, either line or the switching frequency. In both G2V and V2G operations, it is assumed that the primary coil current remains at a constant amplitude sinusoidal waveform. Consequently, the modulation of fluctuating power should be accomplished through control of the primary voltage. The fluctuating power can be obtained using the primary voltage. Utilizing equations (20) and (21), we can define the fundamental voltage reference as follows:

$$v_p^{\wedge *} = V_p^* \left(1 + \cos(2\omega_g t)\right) \tag{22}$$

where, V_p^* value substitute in the equation below,

$$v_p^{\wedge *} = \frac{P_{mean}^* M \omega_0 \pi}{2 V_{BAT}} \left(1 + \cos(2\omega_g t)\right) \tag{23}$$

Using Phase-Locked Loop (PLL) synchronization at the grid measurement system the cosine waveform can be obtained from the preceding equation (23) [22]. Similarly, the Magnitude to Voltage of the Battery Voltage ($M/(V_{BAT})$) is obtained with peak current measurement at the primary coil (24).

$$\frac{M}{V_{BAT}} = \frac{4}{\pi \omega_0 i_p^{\wedge}} \tag{24}$$

From the steady-state measurements of the primary side, it is not easy to extricate M and V_{BAT} separately, as the limits of both parameters are relatively large, and require alternate techniques for a precise V_{BAT} estimation. Using equation (20), the duty cycle expression for the primary side can be calculated as follows

$$\delta_p = \frac{2}{\pi} a \sin\left(\frac{\pi v_p^{\wedge *}}{4 v_r}\right) \tag{25}$$

B. SECONDARY SIDE PSM CONTROL

The secondary rectifier's duty cycle (PWM) is controlled by a Phase Shifted Pulse-Width Modulation (δs) in the secondary-side control approach. An unconstrained square-wave modulation can be used to produce a primary current with a changeable amplitude by modulating the voltage of the secondary side. The secondary coil current can be utilized for the PLL input in case of failure at the on-board system to measure grid voltage. To put it another way, the secondary voltage reference needs to meet these requirements:

$$v_s^{\wedge *} = V_s^{\wedge}[\sin(\omega_g t)] = \frac{P_{mean}^* M \omega_o \pi}{V_{grid}}[\sin(\omega_g t)] \tag{26}$$

As obtaining both variables independently is difficult, the M/V_{grid} value can be approximated using the secondary peak current values (24). It is possible to estimate the coupling factor based on a relatively narrow range of grid voltage amplitude in this case

$$\frac{M}{v_r} = \frac{4}{\pi \omega_0 i_s^{\wedge}} \tag{27}$$

By integrating with equation (6), we can calculate the duty cycle from the secondary side with the equation as:

$$\delta_s = \frac{2}{\pi} a \sin\left(\frac{\pi v_s^{\wedge *}}{4 V_{BAT}}\right) \tag{28}$$

Moreover, every switching device's pulse patterns are provided and differentiated among switches to function as switching frequency f_s and those that operate at line frequency [24], [25].

C. PHASE SHIFT PWM TECHNIQUES FOR INVERTERS

Phase-shift control proves effective for H-bridge converters, thanks to their remarkable efficiency, minimal electromagnetic interference (EMI), and the absence of voltage fluctuation concerns. Generally, when aligning the converter switching angular frequency with the resonant tank's angular resonance frequency, the PSM is formulated as follows,

$$\omega = \frac{1}{\sqrt{L_1 C_1}} = \frac{1}{\sqrt{L_2 C_2}} \quad (29)$$

Exploring the realm of inverter technology, the switches $(S_{P1}\text{-}S_{P4})$ and $(S_{S1}\text{-}S_{S4})$ symbolize the switches on both the primary and secondary sides, alongside their corresponding control signals. The primary and secondary sides' internal phase-shift angles (α, β) are the control signal to match the DC-link voltage by controlling the time interval. Adjusting the phase delay(φ) of the secondary and primary control signals brings suitable control over the power transfer. Because of the erratic wireless communication latency and clock differences between the controllers, the two independent controllers cannot be initiated at the same time. Delay takes on the characteristics of an uncertain phase delay as a result of the unpredictable initiation instructions. The relative phase shift angle (γ) represents the distance between the center point of the secondary voltages V_S, and primary voltage V_P. The subsequent equation elucidates the connection among $(\alpha, \beta, \text{and } \gamma)$.

$$\gamma = \varphi + \varphi_{delay} - \frac{\alpha}{2} + \frac{\beta}{2} \quad (30)$$

The influence of internal phase-shift angles of the secondary and primary sides (α, β) on the relative phase-shift angle (γ) can be seen from the above equation. The BWPT system power transfer can be effectively directed by varying (γ) or in turn controlled by varying α and β. The PWM signal generated by the primary side controller for the switches $(S_{P1}\text{-}S_{P3})$ has $\alpha/2$ leading (lagging) phase angle concerning clock pulse. The delay angle (φ) between the primary and secondary controller clocks is used for the secondary controller's controllable angle. For controlling the secondary side, the phase angle of $(\varphi + \beta/2)$ and $(\varphi\text{-}\beta/2)$ is used to generate the control signal for the switch $(S_{S1}\text{-}S_{S3})$. Hence, the primary and secondary side control signals for the converters with respective phase-shift angle variations are indicated as

$$\gamma = \varphi_{delay} + \varphi \quad (31)$$

For obtaining maximum power transfer efficiency for the BWPT system, the discharging mode's value of $3\pi/2$ and charging mode's value of (γ) is set to $\pi/2$. This adjustment is easily achieved by regulating (ϕ). By modifying this value, the system's transfer power can be controlled to alter both its direction and magnitude. Further, the dead-time effect, the internal phase-shift angles, and the association between the amount of transfer power need to be considered. In this case, the values that must be calculated to achieve the desired transfer power become critical.

D. BIFURCATION

The literature extensively discusses bifurcation situations, and designers typically attempt to prevent this problem by designing coils and resonant correction in accordance with operating conditions. Numerous elements, including the coupling factor, transmitted power, compensatory capacitor, and the ratio of coil self-inductances, should be considered in order to avoid bifurcation. A system's ability to function in both directions may restrict the likelihood of avoiding certain problems, contingent on the particular needs of the system. The efficacy of the BWPT system, employing recommended control strategies, is illustrated in Figure 10, highlighting the influence of the coupling factor (k) and switching frequency on system performance. This resonant inverter demonstrates the capability to operate in various regions, including inductive, Zero Voltage Switching (ZVS), and Zero Current Switching (ZCS), all necessitating hard switching.

Bifurcation plays a pivotal role in determining the switching modes of the resonant inverter, contingent on the frequency-dependent load impedance. Consequently, the bifurcation point holds significant sway over system performance, particularly concerning power losses in semiconductors, thereby exerting a substantial impact on system efficiency.
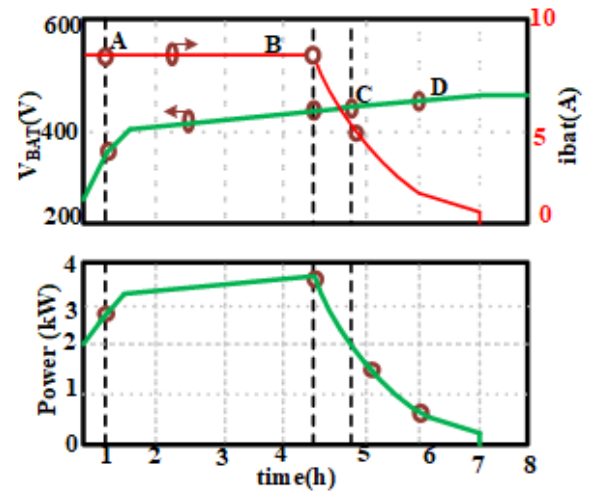

FIGURE 10. Operating points of the wireless charger.

Thus, the bifurcation limits of the proposed system can be identified as follows

$$P_{Limit} = \frac{\hat{V}_s^2}{2\omega_0 L_s} K \quad (32)$$

$$K_{Limit} = \frac{\hat{V}_s^2}{2\omega_0 L_s P} \quad (33)$$

$$x_{limit} = \left(\frac{\hat{v}_p}{\hat{v}_s}\right) \quad (34)$$

where x is the coil inductance ratio, which is defined as

$$x = \frac{L_p}{L_s} \qquad (35)$$

For G2V operation is considered to analyze the bifurcation by expanding the input impedance expression

$$Z_{in} = \frac{\vec{v}_p}{\vec{i}_p} \qquad (36)$$

The load resistance AC value can be calculated from the secondary side as follows

$$R_{SAC} = \frac{\hat{vs}}{\hat{is}} \qquad (37)$$

The output equivalent resistance determines the resistance of the primary side controller when it is implemented as follows:

$$R_{SAC} = \frac{\frac{4}{\pi} V_{BAT}}{\frac{\pi}{2} i_{BAT}} = \frac{8}{\pi^2} R_{2,DC} \qquad (38)$$

The corresponding AC resistance, on the other side, varies with the duty cycle when employing the secondary control technique [24]

$$R_{SAC} = \frac{8}{\pi^2} R_{2,DC} \sin^2\left(\frac{\delta_s \pi}{2}\right) \qquad (39)$$
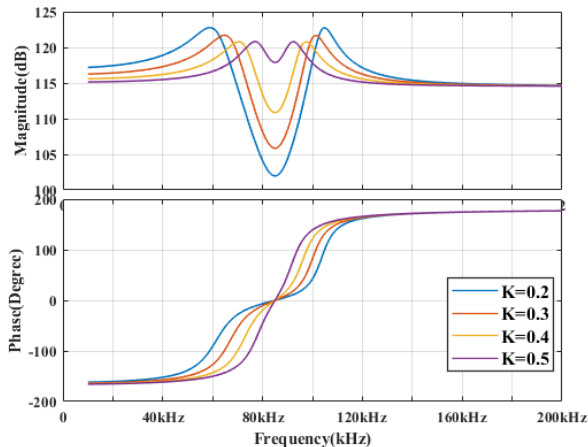
FIGURE 11. Bode diagram illustrating the input impedance (Zin) for various coupling factors (k) with primary control.

At the certain instance of the resonance, the input impedance is characterized as follows

$$Z_{in} = \frac{\omega_0^2 k^2 L_p L_s}{R_{SAC}} \qquad (40)$$

A bode diagram showing the input impedance magnitude vs switching frequency is shown in Figure 10. Zero Voltage Switching (ZVS) is made possible via inductive action, which is indicated by a positive phase [26]. On the other hand, a capacitive zone requires hard-switching since it correlates with a negative phase. Examining the bifurcation behavior of primary-side control reveals that bifurcation issues do not impact primary-side control, even in the presence of large

coupling factor values, as Figure 11 illustrates. However, bifurcation issues arise in secondary-side control when dealing with large coupling factors (k > 0.3), as depicted in Figure 12.
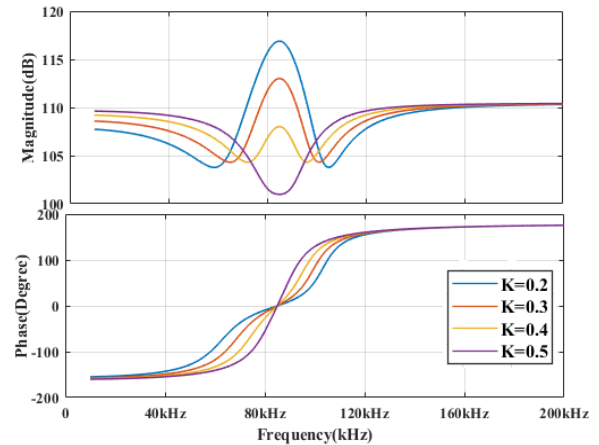

FIGURE 12. Bode diagram illustrating the input impedance (Zin) for various coupling factors (k) with secondary control.

Even at high coupling factors, the primary-side control does not display bifurcation; in contrast, when the coupling factor is large, the secondary-side control does. Additionally, the bifurcation is examined for the various values of the coupling coefficients, which range from K=0.2 to K=0.5. For k=0.2, the power, coupling, and voltage ratio are near the bifurcation limit. When K=0.3, there is no bifurcation since the secondary voltage is greater than the primary voltage and the power and coupling are both below the prescribed limitations. For K=0.4 & 0.5, respectively, there is no bifurcation because the power and coupling are both beyond the required limits and the secondary voltage is lower than the primary voltage. As the coupling coefficient increases beyond the critical coupling value, the frequency gets divided into two components as higher angular frequency (ω_H) and lower angular frequency (ω_L). When the coupling coefficient equals the critical coupling coefficient (K_C), both frequencies merge and the phase angle is zero. An additional reduction in the coupling coefficient eliminates both phase angle frequencies. Therefore, the coupling coefficient should be less than the critical coupling coefficient for optimal gain and bifurcation-free operation.

E. THD AND PFC CONTROL
For accomplishing the ZVS operation of the inverter, the resonant circuit is used to be operated close to the resonant frequency but with little outside the point to maintain the inductive energy in the circuit. However, for the BWPT systems to maintain constant output it is necessary to keep enough induced voltage at the secondary coil. The distinction lies in the differences between unrestrained output voltage operation and controlled operation. When the switching frequency is not precisely in resonance and fails to generate
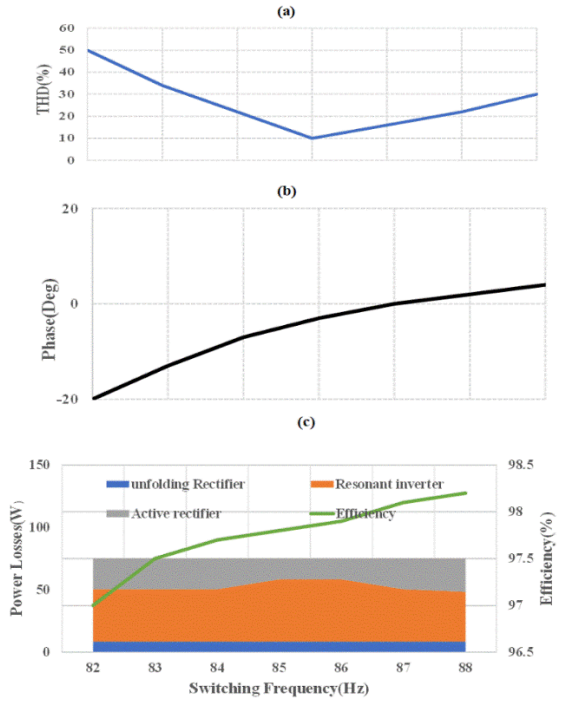
FIGURE 13. Primary-side control strategy effectiveness about coupling factor and switching frequency a) Input current THD b) Phase angle at Primary side c) Efficiency and Power loss.

enough voltage to bias the semiconductor devices, the secondary rectifier may exhibit nonlinear behaviour.

This nonlinearity arises due to the minimal induced voltage, affecting the input current Total Harmonic Distortion (THD) when employing two control techniques. This becomes especially critical during grid voltage zero-crossing or low-load circumstances, such as the last section of continuous voltage at the D point. The primary control strategy falls short of generating sufficient voltage near the grid zero-crossing. Consequently, active power transfer is absent, and the current operates nonlinearly, leading to inadequate Power Factor Correction (PFC). However, the THD characteristics demonstrate significant improvements in the resonance frequency when utilizing primary-side control. Figure 13 illustrates that by adjusting the switching frequency, there is a noticeable improvement in Total Harmonic Distortion (THD). This improvement is attributed to the minimization of the voltage decrease in the resonant tank, leading to a higher induced voltage. In contrast, deviations from resonance have a lesser impact on secondary control, maintaining a relatively low THD across the frequency range analyzed in Figure 14. As a result, primary control operates smoothly without encountering bifurcation, contributing to increased efficiency, particularly above the resonance frequency. Efficiency gains are ascribed to Zero Voltage Switching (ZVS) and the concomitant decrease in inverter power losses. Conversely, bifurcation occurs in secondary-side control, resulting in an enhanced efficiency characteristic below the resonance frequency.
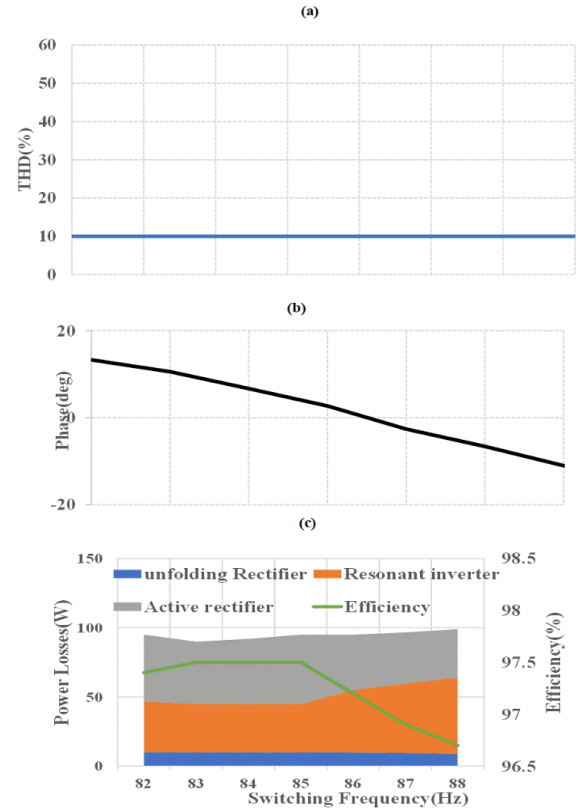

FIGURE 14. Secondary-side control strategy effectiveness about coupling factor and switching frequency a) Input current THD b) Phase angle at Primary side c) Efficiency and Power loss.

F. POWER LOSS

The evaluation of the BWPT system's performance in both G2V and V2G modes involves a comprehensive analysis of various system components and an examination of the associated power losses. The semiconductor switching loss that occurs at each stage of the power converter is only the primary loss considered in the evaluation. In addition, the carrier signal which is in phase with the current at the secondary also adds the switching losses to the secondary rectifier. Furthermore, the selection of the switching frequency near the resonant frequency minimizes the frequency bifurcation. The total system efficiency, expressed as the ratio of the system's fundamental equation concerning output power to input power, is presented in equation (41).

$$\eta_{total} = \eta_{rectifier} \times \eta_{HFPC} \times \eta_{compensation} \times \eta_{pad}$$
$$\times \eta_{compensation} \times \eta_{HFSC} \times \eta_{Bidirectional(DC-DC)}$$
$$= \frac{p_{output}}{p_{input}} = \frac{p_{input} - p_{losses}}{p_{input}} \quad (41)$$

The Total power losses are calculated by adding the front-end converter (FEC), High-frequency primary converter (HFPC), compensation networks (CN), charging pad (CP), High-frequency secondary converters (HFSC), and the

Bidirectional DC-DC converters.

$$P_{loss} = P_{l-rectifier} + P_{l-HFPC} + P_{l-compensation}$$
$$+ P_{l-pad} + P_{l-compensation} + P_{l-HFSC}$$
$$+ P_{l-bidirectional(DC-DC)converters} \quad (42)$$
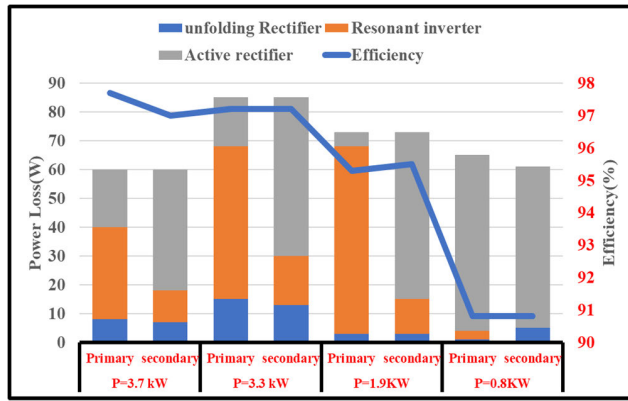

FIGURE 15. The power loss and efficiency performance at different operating points at 85 kHz and k=0.2.

It is possible to calculate the charging pad losses using the following factors: rated voltage and current from, angular frequency (ω), inductance (L), windings of the AC resistance coils from (43)

$$P_{l-coupler} = P_{l-winding} + P_{l-core} \quad (43)$$

The power losses across the charging pads are given by the equation (44)

$$P_{l-coupler} = (I_{rms}^2 \times r_{ac}) + (c_m \times f_{sw}^{\alpha} \times \beta^{\beta}) \quad (44)$$

From the Steinmetz equation, considering system frequency (f_s), flux density (B), and coupling coefficient values, it is possible to ascertain the charging pad's core loss. The losses of the inverter can be calculated by approximating the switching and conduction losses of the operational SIC MOSFET. Similarly, the diode's losses might be determined by adding up these losses.

$$P_{l-MOSFET}$$
$$= P_{l-conduction} + P_{l-switching} + P_{l-driving}$$
$$= \left(R_{ds}(on) \times I_{rms,M}^2\right) + (((V_{DS} \times I_{rms,M} \times t_{on,M})$$
$$+ (V_{DS} \times I_M \times t_{off,M})) \times f_{sw}) + (2 \times V_{gs} \times Q_{gs}) \quad (45)$$

where,

$$P_{l-MOSFET} = P_{l-conduction} + P_{l-switching}$$
$$+ ((V_F \times I_{avg,D}) + (R_d \times I_{rms,D}^2))$$
$$+ (Q_{rr} \times V_{diode}) \times f_{sw} \quad (46)$$

According to equation (45), the commutation voltage is denoted by V_{DS}, the on-state resistance of the MOSFET switches is represented by $R_{ds,ON}$, the current flowing through the MOSFET switches is represented by I_{rms}^2, M, and

the gate to source terminal voltage and charge are indicated by V_{gs} and Q_{gs}. The diode voltage is represented by V_D and the forward voltage by V_F. The $I_{avg,D}$ and $I_{rms,D}^2$ are the average and rms current values of the diode respectively. According to ZVS, the primary control functions without bifurcation achieve increased efficiency above resonance frequency to decrease inverter power losses. In addition, the secondary side control displays bifurcation, resulting in improved efficiency characteristics below the resonance frequency. Since the load's input impedance is always inductive above resonance frequency, getting ZVS in unbifurcated systems is quite straightforward, much like with the primary side control approach. A detailed overview of the system's overall performance and power losses at each level can be found in Figure 15. These computations only account for the power losses that the semiconductor devices experience. As mentioned earlier, the carrier signal which is in phase with the current at the secondary also adds the switching losses to the secondary rectifier. Also, the selection of the switching frequency near the resonant frequency minimizes the frequency bifurcation at the secondary-side control. Although the distribution of these losses varies, the efficiency findings show that both control systems occur equivalent overall power losses.

VI. RESULTS AND DISCUSSION

For the proposed system the simulation study and experimental verifications are performed for the 3.7 kW power rating as per the specifications mentioned in Table 1. The MATLAB simulation is performed for both the G2V and V2G modes of operation. The essential parameters such as voltage, current at the grid side, transmitter and receiver coil side as well as inverter end are measured. The simulation settings utilized are in compliance with the specifications given; specifically, the output voltage at secondary inverter side (V_{out}) is 420 V, the input AC voltage (V_{Grid}) is 325 V. The coupling coefficient (K) is of 0.4 and an 85 kHz switching frequency (f_s) are considered. The system components consist of the following components: the capacitance filter (C_0), the self-inductance of the secondary coil (L_S), the secondary side series compensation capacitor (C_S), the self-inductance of the primary coil (L_P), and the capacitor for primary side series compensation (C_P). The mutual inductance (M) is considered as 46.5μH. This extensive simulation research guarantees a detailed investigation on the performance of the suggested dual-phase shift Pulse Width Modulation (PWM) approach under various operational conditions.

A. SIMULATION RESULTS FOR G2V SIDE

Initially the G2V operating simulation mode is run first, considering the grid frequency of 50Hz and a magnitude of grid supply voltage 325V. Figure 16(a) shows the sinusoidal change of the nominal grid input voltages. The primary side converter voltage and current are illustrated in Figure 16(b), the waveform indicates that the THD during the G2V mode of operation with primary side control is less. Whereas, the primary coil current and the voltage plotted

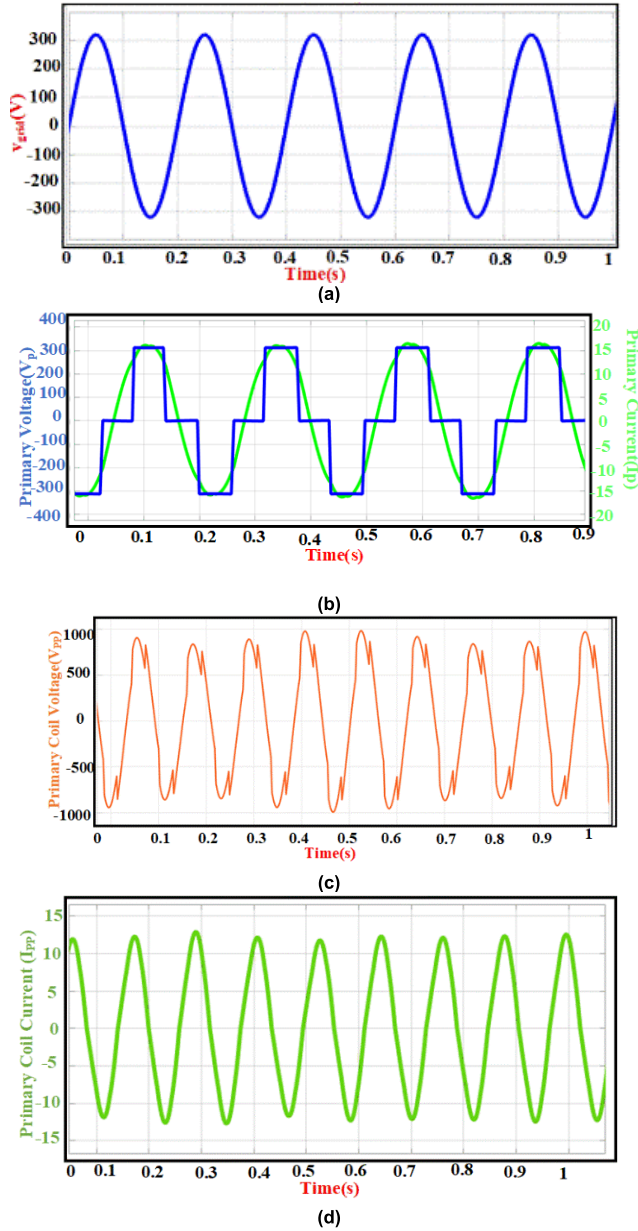in Figure 16(c) and (d) shows that the presence of voltage harmonics.

FIGURE 16. (a)The Grid Input Voltage (b) Primary side Converter voltage control (V_{pp}) Current (I_{pp}) (c) Primary coil voltage (V_{pp}) across the transmitter pads (V_{pp}) (d) The Primary coil current across the transmitter pads (I_{pp}).

FIGURE 17. (a) Secondary side Converters voltage control (V_{SS}) Current (I_{SS}) Waveforms (b) Secondary coil voltage (V_{SS}) across the Receiver pads (c) Secondary coil Current (I_{SS}) across the Receiver pads.

Meanwhile, when it comes to the primary coil side, the modulated voltage (V_{pp}) is close to 940 V, and the modulated current (I_{pp}) is of 12A. Whereas the secondary side voltage and current are shown in Figure 17(a) is of at 220V and 18A by using unregulated control at the secondary side. Similarly, the secondary coil side modulated voltage (V_{SS}) is of 1000 V, and the secondary coil side modulated current (I_{SS}) is of 8 A. The waveform at the secondary side indicates that the presence of voltage harmonics is higher than the current
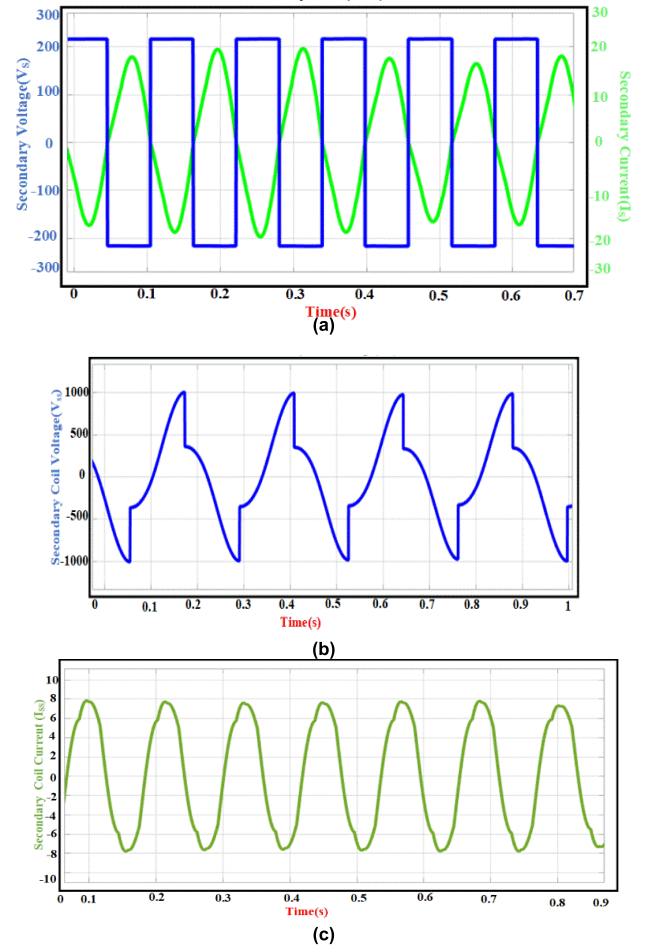
harmonics level at the coil end. Also, at the output of the secondary converter the THD level is minimized with the presence of compensation resonance capacitance.

The results of the simulation study for the G2V operation indicates that the primary side control provides better control over the THD and bifurcation at the primary and secondary end. On the other side, the use of uncontrolled operation at the secondary side brings same PFC during G2V operation. The enhancement in the PFC could be evident during the secondary control operation with the V2G operation.

B. SIMULATION RESULTS FOR V2G SIDE
The V2G side of simulation study is performed with the control over the secondary converter and without modulating the primary side converter. The design parameters are followed as same for the G2V operation except the control flow changes. Figure 18(a) shows the primary side unregulated square-wave modulation converter voltage and current. The peak value of the primary side voltage (V_{pp}) and primary current (I_{pp}) is of 150V and 10 A respectively. Meanwhile, Figures 18(b) and 18(c) show the sinusoidal current and

fluctuating voltage that are derived from the primary side pad voltage and current. The current THD are minimum at the primary side compared to the voltage. Moreover, the PFC at the primary side with the control of secondary end is enhanced in V2G mode of operation.
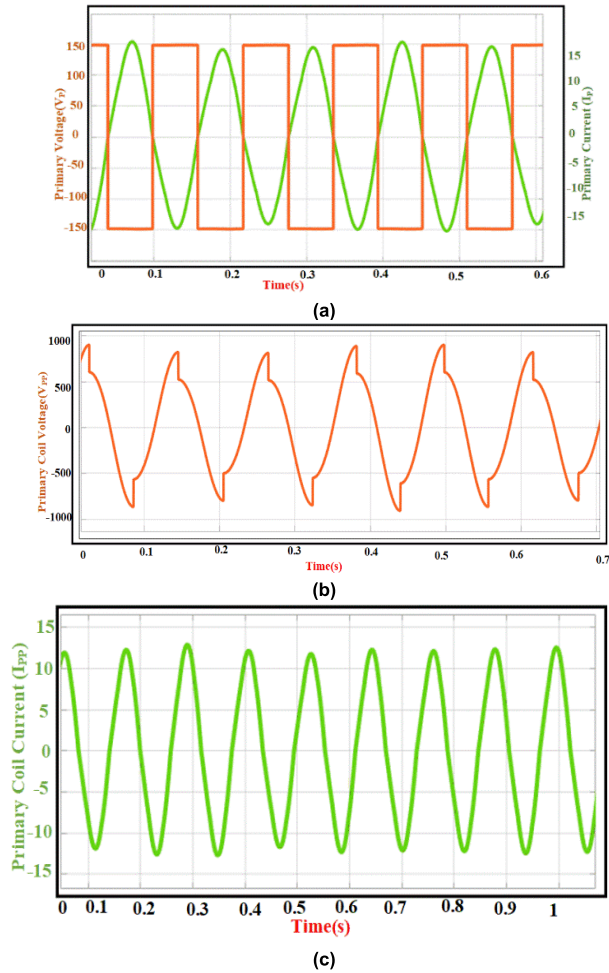

FIGURE 18. (a) Converter voltage(V_{PP}) Current (I_{PP}) at the primary side (b) Voltage (V_{PP}) across the primary pads (c) Primary coil Current (I_{PP}).

The secondary side measured parameters are represented in Figures 19(a) through 19(c). Figure 19(a) shows the secondary side converter voltage and current with the amplitude of 310 V and 8 A. Similarly, the secondary side coil voltage and current represented in Figure 19(b) and Figure 19(c). The magnitude of the coil voltage and current are of 600 V and 8 A respectively. The secondary side control with the V2G mode of operation shows the improved PFC over the primary side control. Whereas, the THD and bifurcation are unchanged in V2G mode.

C. EXPERIMENTAL RESULTS FOR G2V CONTROL

A lab scale prototype module for bidirectional WPT systems is shown in Figure 20. It is designed with two identical H-Bridges that serve as the primary and secondary side converters, coupling coils, resonant capacitors, and a
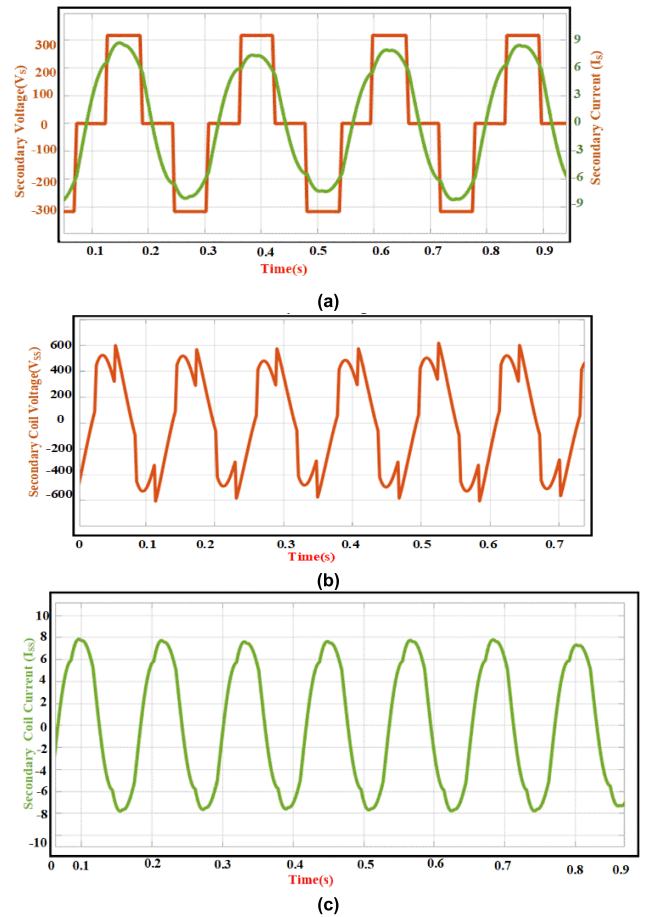

FIGURE 19. (a) Secondary side Converter voltage control (V_{SS}) Current (I_{SS}) (b) Secondary side coil voltage (V_{SS}) across the Receiver Pads (c) Secondary side coil Current (I_{SS}) across the Receiver Pad.
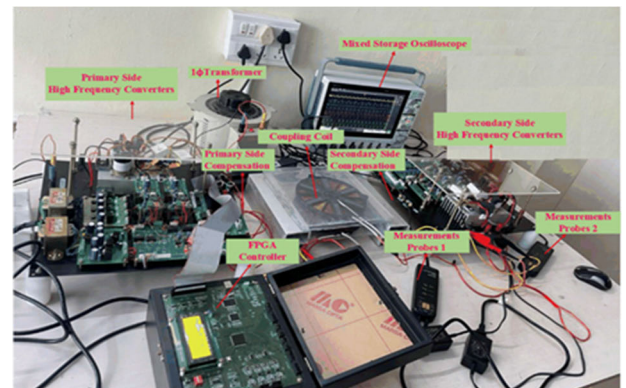

FIGURE 20. Experimental prototype module of bidirectional WPT.

Spartan 6 Field Programmable Gate Array (FPGA) controller that controls each converter's PWM pulse separately. The H bridge converters are designed using N channel SIC MOSFET(MSC360SMA120B) and the compensating resonant capacitors of KMET(PHE450XD5100JD15R06L2) film category. Both H-bridge converters have four SIC MOSFETs and four SIC Schottky diodes. The duration
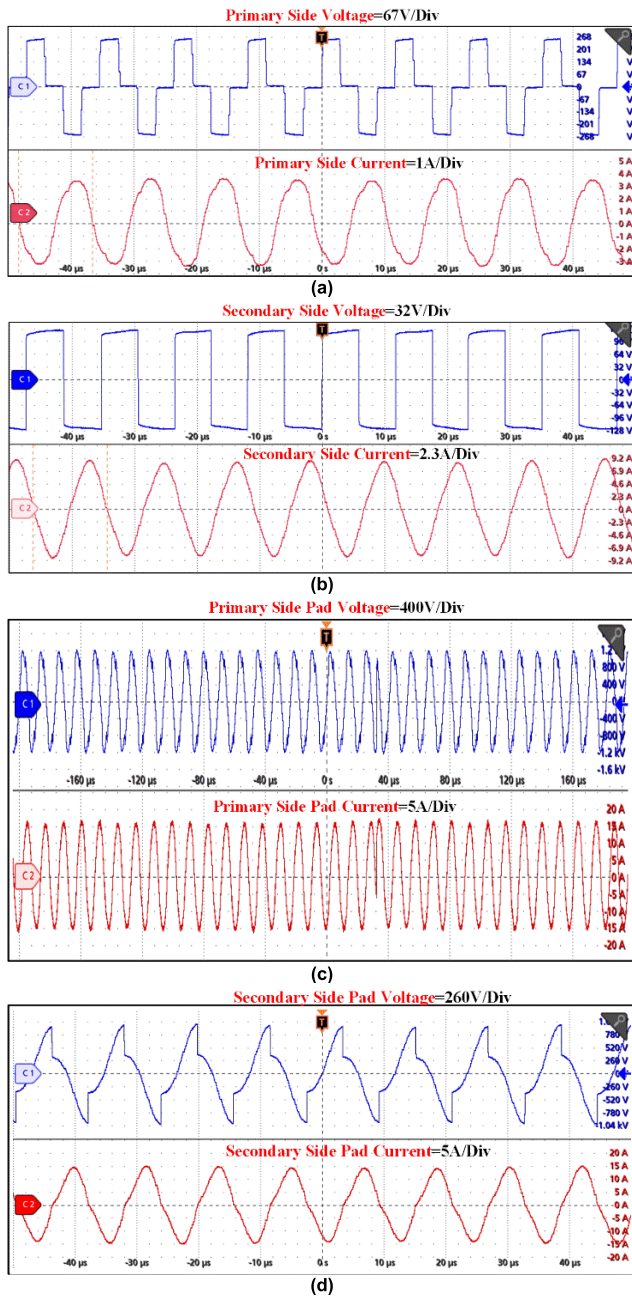
FIGURE 21. G2V Control (a) Converter voltage and current at primary (b) Converter voltage and current at secondary (c) Coil voltage and current at primary(d) Coil voltage and current at secondary.

FIGURE 22. V2G Control (a) Converter voltage and current at primary (b) Converter voltage and current at secondary (c) Coil voltage and current at primary(d) Coil voltage and current at secondary.

is 11.764 microseconds, and the switching frequency is 85 kHz. The primary and secondary coils are designed with the identical low resistance multi strand wire of e-Infinity type with radial core placement. The coil dimension is of $1.2 \times 0.5 \times 1.2$ cm. Then, each stage of the bidirectional module system is analyzed in terms of its grid and converter parameters and power constraints.

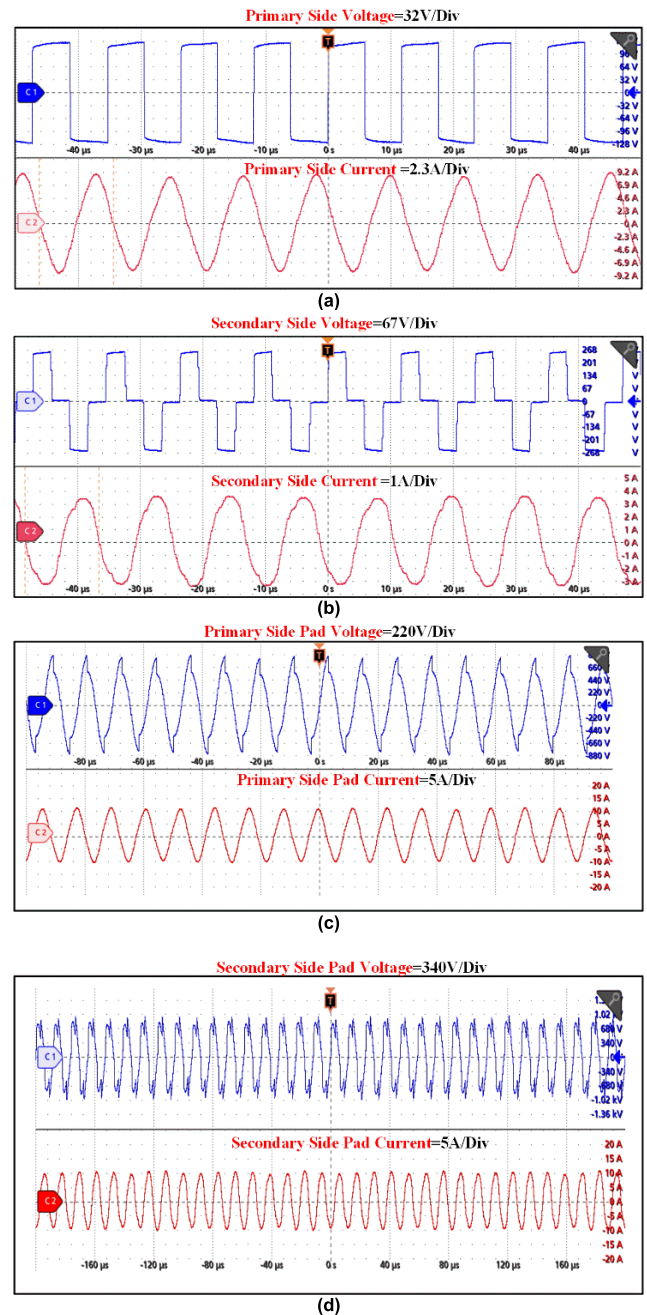Figures 21(a)and 21(b) illustrate the high-frequency converter on the primary side as well as the secondary side voltage and current. Since the voltage and current are clearly in phase, the power factor stays closer to 1. Additionally, the voltage and current waveforms for both pads (transmitter and receiver) are shown in Figures 21(c) and 21(d). Half of the voltage across the secondary side is applied to the primary side voltage control. The current across the secondary side is equal to the current on the primary side in a similar manner. During the G2V mode of operation the primary side THD are minimum with good control over the power factor.

D. EXPERIMENTAL RESULTS FOR V2G CONTROL

In this section, the experimental basis of the proposed topology for V2G side control is illustrated. Figures 22(a) and 22(b) illustrate the high-frequency converter for controlling voltage and current. Compared to the secondary side control, the voltage across the primary side control is twice as high. Similarly, the value of the primary side current is half that of the secondary. Also shown in Figures 22(c) and 22(d) are the voltage and current waveforms for the transmitter and receiver pads. A primary side control's voltage is 1.5 times higher than a secondary side control's voltage. Like the secondary side current, the primary side current is of equal size.

Both side control systems were assessed to make it easier to compare the THD, efficiency, and power factor (PF) from the above figures. The displacement and distortion power factors have both been considered when computing the total power factor. Nevertheless, the measurements show that the THD value stays at 10% and that the measured PF values are continuously close to unity. As a result, it has been shown that these experimental results support the findings of the simulation and show how effective the suggested techniques are for the BWPT system.

VII. CONCLUSION

The proposed work offers suitable approach to tackle problems that arise in BWPT systems used in EV charging applications. Beyond the constraints of traditional power factor control methods, the suggested dual-phase shift-regulated PWM methodology provides a sophisticated power factor control strategy designed for two-way operations. A thorough analysis is conducted to support the effectiveness of the suggested system, taking into account factors such as power factor, bifurcation, total harmonic distortion (THD), and power losses. Power transfer efficiencies of 94.4% and 90.1%, respectively, for a 3.7 kW power rating at an 85 kHz operating frequency are demonstrated in simulation and experimental validation tests for G2V and V2G modes. The V2G mode of operation with the dual phase shift control offers the enhanced power factor control without changing the THD and bifurcation factor. Whereas, the G2V mode of operation with the primary control provides the enhancement in the THD and bifurcation. The development of smart and sustainable energy systems depends on improving control mechanisms, as this study emphasizes. It not only makes EV incorporation into smart grids easier, but it also improves BWPT systems' overall efficiency. In order to support different power ratings and frequencies, future research in BWPT systems concentrate on improving the scalability and adaptability of the suggested dual-phase shift Pulse Width Modulation (PWM) technology. Examining the incorporation of cutting-edge technology, such machine learning or artificial intelligence, may help refine control strategies for better efficiency and performance of the system. Furthermore, investigating the possible incorporation of energy storage systems into the bidirectional power transmission structure may improve the overall dependability and grid stability of the system.

REFERENCES

[1] M. Venkatesan, N. Rajamanickam, P. Vishnuram, M. Bajaj, V. Blazek, L. Prokop, and S. Misak, "A Review of compensation topologies and control techniques of bidirectional wireless power transfer systems for electric vehicle applications," *Energies*, vol. 15, no. 20, Oct. 1, 2022, doi: 10.3390/en15207816.

[2] Q. He, Q. Luo, K. Ma, P. Sun, and L. Zhou, "Analysis and design of a single-stage bridgeless high-frequency resonant AC/AC converter," *IEEE Trans. Power Electron.*, vol. 34, no. 1, pp. 700–711, Jan. 2019.

[3] M. Kim, D.-M. Joo, and B. K. Lee, "Design and control of inductive power transfer system for electric vehicles considering wide variation of output voltage and coupling coefficient," *IEEE Trans. Power Electron.*, vol. 34, no. 2, pp. 1197–1208, Feb. 2019, doi: 10.1109/TPEL.2018.2835161.

[4] X. Wang, J. Xu, M. Leng, H. Ma, and S. He, "A hybrid control strategy of LCC-S compensated WPT system for wide output voltage and ZVS range with minimized reactive current," *IEEE Trans. Ind. Electron.*, vol. 68, no. 9, pp. 7908–7920, Sep. 2021, doi: 10.1109/TIE.2020.3013788.

[5] X. Qu, H. Chu, S.-C. Wong, and C. K. Tse, "An IPT battery charger with near unity power factor and load-independent constant output combating design constraints of input voltage and transformer parameters," *IEEE Trans. Power Electron.*, vol. 34, no. 8, pp. 7719–7727, Aug. 2019, doi: 10.1109/TPEL.2018.2881207.

[6] X. Liu, N. Jin, X. Yang, K. Hashmi, D. Ma, and H. Tang, "A novel single-switch phase controlled wireless power transfer system," *Electronics*, vol. 7, no. 11, p. 281, Oct. 2018, doi: 10.3390/electronics7110281.

[7] V. Shevchenko, O. Husev, R. Strzelecki, B. Pakhaliuk, N. Poliakov, and N. Strzelecka, "Compensation topologies in IPT systems: Standards, requirements, classification, analysis, comparison and application," *IEEE Access*, vol. 7, pp. 120559–120580, 2019.

[8] D. Xu, C. Zhao, and H. Fan, "A PWM plus phase-shift control bidirectional DC–DC converter," *IEEE Trans. Power Electron.*, vol. 19, no. 3, pp. 666–675, May 2004, doi: 10.1109/TPEL.2004.826485.

[9] R. Bosshard, J. W. Kolar, J. Mühlethaler, I. Stevanovic, B. Wunsch, and F. Canales, "Modeling and η–α -Pareto optimization of inductive power transfer coils for electric vehicles," *IEEE J. Emerg. Sel. Topics Power Electron.*, vol. 3, no. 1, pp. 50–64, Mar. 2015, doi: 10.1109/JESTPE.2014.2311302.

[10] R. Bosshard and J. W. Kolar, "Inductive power transfer for electric vehicle charging: Technical challenges and tradeoffs," *IEEE Power Electron. Mag.*, vol. 3, no. 3, pp. 22–30, Sep. 2016, doi: 10.1109/MPEL.2016.2583839.

[11] M. Neath, "Bidirectional inductive power transfer system: Analysis and control," Ph.D. dissertation, Univ. Auckland, Auckland, New Zealand, 2013. [Online]. Available: http://hdl.handle.net/2292/22756

[12] M. Mohammad, O. C. Onar, G.-J. Su, J. Pries, V. P. Galigekere, S. Anwar, E. Asa, J. Wilkins, R. Wiles, C. P. White, and L. E. Seiber, "Bidirectional LCC–LCC-compensated 20-kW wireless power transfer system for medium-duty vehicle charging," *IEEE Trans. Transport Electrific.*, vol. 7, no. 3, pp. 1205–1218, Sep. 2021, doi: 10.1109/TTE.2021.3049138.

[13] S. A. Gorji, H. G. Sahebi, M. Ektesabi, and A. B. Rad, "Topologies and control schemes of bidirectional DC–DC power converters: An overview," *IEEE Access*, vol. 7, pp. 117997–118019, 2019, doi: 10.1109/ACCESS.2019.2937239.

[14] V. Juliet, S. Padmanaban, and L. Mihet-Popa, "Frequency splitting elimination and cross-coupling rejection of wireless power transfer to multiple dynamic receivers," *Appl. Sci.*, vol. 8, no. 2, p. 179, Jan. 2018, doi: 10.3390/app8020179.

[15] T. Taipei, X. Xu, A. M. Khambadkone, and R. Oruganti, "A soft-switched back-to-back Bi-directional DC/DC converter with a FPGA based digital control for automotive applications," in *Proc. 33rd Annu. Conf. IEEE Ind. Electron. Soc.*, 2007, pp. 262–267.

[16] K. Colak, E. Asa, M. Bojarski, D. Czarkowski, and O. C. Onar, "A novel phase-shift control of semibridgeless active rectifier for wireless power transfer," *IEEE Trans. Power Electron.*, vol. 30, no. 11, pp. 6288–6297, Nov. 2015, doi: 10.1109/TPEL.2015.2430832.

[17] H. Wu, Y. Lu, T. Mu, and Y. Xing, "A family of soft-switching DC–DC converters based on a phase-shift-controlled active boost rectifier," *IEEE Trans. Power Electron.*, vol. 30, no. 2, pp. 657–667, Feb. 2015, doi: 10.1109/TPEL.2014.2308278.

[18] H. Xiao and S. Xie, "A ZVS bidirectional DC–DC converter with phase-shift plus PWM control scheme," *IEEE Trans. Power Electron.*, vol. 23, no. 2, pp. 813–823, Mar. 2008, doi: 10.1109/TPEL.2007.915188.

[19] Y. Yang, Y. Benomar, M. El Baghdadi, O. Hegazy, and J. Van Mierlo, "Design, modeling and control of a bidirectional wireless power transfer for light-duty vehicles: G2 V and V2G systems," in *Proc. 19th Eur. Conf. Power Electron. Appl.*, Sep. 2017, pp. P1–P12, doi: 10.23919/EPE17ECCEEurope.2017.8099387.

[20] S. Liu, J. Su, and J. Lai, "Accurate expressions of mutual inductance and their calculation of Archimedean spiral coils," *Energies*, vol. 12, no. 10, p. 2017, May 2019, doi: 10.3390/en12102017.

[21] K. Aditya, "Analytical design of Archimedean spiral coils used in inductive power transfer for electric vehicles application," *Electr. Eng.*, vol. 100, no. 3, pp. 1819–1826, Sep. 2018, doi: 10.1007/s00202-017-0663-7.

[22] Y. Yang, J. Cui, and X. Cui, "Design and analysis of magnetic coils for optimizing the coupling coefficient in an electric vehicle wireless power transfer system," *Energies*, vol. 13, no. 16, p. 4143, Aug. 2020, doi: 10.3390/en13164143.

[23] X. Liu, C. Xia, and X. Yuan, "Study of the circular flat spiral coil structure effect on wireless power transfer system performance," *Energies*, vol. 11, no. 11, p. 2875, Oct. 2018, doi: 10.3390/en11112875.

[24] A. Garcia-Bediaga, A. Avila, I. Alzuguren, A. Sanchez, and A. Rujas, "Power factor corrector control strategies of a bidirectional wireless battery charger with an unfolding active rectifier," *IEEE J. Emerg. Sel. Topics Power Electron.*, vol. 11, no. 1, pp. 396–406, Feb. 2023, doi: 10.1109/JESTPE.2022.3164720.

[25] X. Wang, M. Leng, L. He, and S. Lu, "An improved LCC-S compensated inductive power transfer system with wide output voltage range and unity power factor," *IEEE Trans. Transport. Electrific.*, early access, doi: 10.1109/TTE.2023.3297623.

[26] T. Bouanou, H. El Fadil, A. Lassioui, O. Assaddiki, and S. Njili, "Analysis of coil parameters and comparison of circular, rectangular, and hexagonal coils used in WPT system for electric vehicle charging," *World Electric Vehicle J.*, vol. 12, no. 1, p. 45, Mar. 2021, doi: 10.3390/wevj12010045.

R. NARAYANAMOORTHI (Member, IEEE) received the bachelor's degree in electrical engineering and the master's degree in control and instrumentation from Anna University, India, in 2009 and 2011, respectively, and the Ph.D. degree from the SRM Institute of Science and Technology, India, in 2019. He is currently an Associate Professor with the Department of Electrical and Electronics Engineering, SRM Institute of Science and Technology. His research interests include wireless power transfer, electric vehicles, power electronics, artificial intelligence and machine learning in renewable energy systems, and embedded systems for smart sensors.

KAREEM M. ABORAS received the B.Sc., M.Sc., and Ph.D. degrees in electrical engineering from the Faculty of Engineering, Alexandria University, Alexandria, Egypt, in 2010, 2015, and 2019, respectively. His Ph.D. research work is focused on the performance enhancement of renewable energy conversion systems. Currently, he is an Assistant Professor with the Electrical Power and Machines Department, Faculty of Engineering, Alexandria University. He is also a Reviewer of IEEE TRANSACTIONS ON ENERGY CONVERSION, *Electric Power Systems Research*, *Smart Science*, *Alexandria Engineering Journal* (IET), *Energy Reports*, IEEE ACCESS, *Cybernetics and Systems*, *Protection and Control of Modern Power Systems* (MDPI), *Journal of Advanced Research in Applied Sciences and Engineering Technology*, *Cogent Engineering*, and Hindawi journals. His research interests include power electronics, control, drives, power systems, smart grids, microgrids, power quality, optimizations, electric vehicles, machine learning, modeling, fuel cells, HVDC, and renewable energy systems.

MURUGAN VENKATESAN received the B.E. degree in electrical and electronics engineering from the Dhanalakshmi College of Engineering, Chennai, and the M.Tech. degree in power electronics and drives from the Arunai College of Engineering and Technology, Tiruvannamalai. He is currently a Research Scholar with the Department of EEE, SRM Institute of Science and Technology. His research interests include bidirectional wireless power transfer and electric vehicle charging. He is a Lifetime Member of MISTE.

AHMED EMARA was born in Alexandria, Egypt, in 1974. He received the B.S. degree in communication engineering and electro-physics, the M.S. degree in engineering physics, and the Ph.D. degree from the Faculty of Engineering, Alexandria University, Egypt, in 1996, 2003, and 2008, respectively. He is currently an Assistant Professor with the College of Engineering, University of Business and Technology, Jeddah, Saudi Arabia. His research interests include semiconductors, optical devices, and optoelectronics.

• • •